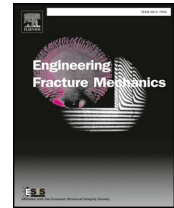




Contents lists available at ScienceDirect

Engineering Fracture Mechanics

journal homepage: www.elsevier.com/locate/engfracmech

The effects of proppant on the near-front behavior of a hydraulic fracture

Alena Bessmertnykh^{a,*}, Egor Dontsov^b, Roberto Ballarini^a^a Department of Civil and Environmental Engineering, University of Houston, Houston, TX 77204, United States^b W.D. Von Gonten Laboratories, 10496 Katy Fwy, Houston, TX 77043, United States

ARTICLE INFO

Keywords:

Hydraulic fracturing
Tip asymptotics
Proppant
Slurry
Porous media

ABSTRACT

The qualitative and quantitative effects of proppant on the near-front region of a hydraulic fracture are investigated by solving the problem of a semi-infinite fracture driven by a slurry of Newtonian fluid with proppant. The results demonstrate that proppant bridging and slurry dehydration cause proppant accumulation near the crack front and, in turn, a pressure difference over the proppant pack that leads to significant fracture widening. Specific attention is paid to the sensitivity of the solution to proppant volume, particle radius, the permeability of the proppant pack, and bridging criterion.

1. Introduction

Unconventional reservoirs are a considerable source of oil and gas. However, before the advent of hydraulic fracturing technology, it was difficult to extract the hydrocarbons from within them because they are comprised of low permeability rocks. Unconventional oil and gas production has significantly improved over the last decades due to a combination of hydraulic fracturing and horizontal drilling techniques [21,3]. The introduction of multiple cracks from a wellbore creates paths along which the hydrocarbons can move from within the matrix to the wellbore and, in turn, can be extracted from the underground. The injected fluid usually contains proppants, granular materials such as sands and ceramics, which prevent complete closure of the cracks after the pumping pressure is released, thus leaving conductive paths for hydrocarbons to flow to the surface. The review of fracturing fluids and their rheology in application to hydraulic fracturing can be found in [2].

The global behavior of a hydraulic fracture (HF) is dominated by the processes occurring near its front. This region can be modeled as a semi-infinite crack in a linear elastic medium propagating steadily under plane strain conditions [40]. Because the problem is two-dimensional, the crack front will henceforth be referred to as the crack tip. A wealth of research has shown that the extension of an HF is dominated by three distinct processes that occur within three regions in the wake of the crack. These processes are characterized as being dominated by either the rock fracture toughness, the fluid viscosity, or fluid leak-off [14]. The solution for the toughness dominated regime originates from linear elastic fracture mechanics (LEFM), a one-parameter theory that dictates crack extension occurs when the stress intensity factor reaches a value equal to the fracture toughness of the matrix material [41]. The solution for the viscosity dominated regime was obtained in [13] and for the leak-off dominated regime in [32]. Both solutions were derived for power-law fluid rheology. A numerical solution that captured all three phenomena for a Newtonian fluid was obtained in [23]. A more efficient computational procedure based on an accurate approximate solution for the general problem was developed in [16]. The approach was based on the removal of the fluid pressure singularity along the crack front, which allowed the use of

* Corresponding author.

E-mail address: abessmertnykh@uh.edu (A. Bessmertnykh).

standard numerical techniques. The same methodology was subsequently applied to solve the general problem that accounts for fluid viscosity, fluid leak-off, and fracture toughness for power-law fluid rheology in [18] and for Herschel-Bulkley fluid rheology in [6]. However, the aforementioned studies of the HF’s near-tip behavior did not include the effects of proppant. An attempt to account for proppant was made in [5] under the assumption that the region in the wake of the crack tip that extends to the fracture is filled with proppant at the maximum concentration, and that the fluid filtrates through the packed proppant according to Darcy’s equation. In this paper, we generalize the formulation by representing the slurry flow within the HF as a multi-phase flow of Newtonian fluid containing a proppant whose concentration is treated as an unknown variable.

Strategies for modeling slurry flows, otherwise called granular suspension flows, include the diffusive flux method [31] and the suspension balance model [35,39,34]. The suspension balance model consists of the balance equations for fluid and particles and accounts for the shear and normal stresses exerted by the particles. Proppant transport has also been modeled using the kinetic theory of granular flows [25,22], in which a statistical particle velocity distribution is assumed and the concept of granular temperature is used to describe slurry flow using statistics (similar to the kinetic theory of gases). Models of proppant transport inside an HF can be characterized using either single-phase or multi-phase approaches, see e.g., review [36] and references therein. The single-phase approach uses the fact that the addition of proppant to the fracturing fluid effectively increases the viscosity of the mixture, and that apart from settling, particles move together with the carrier fluid. This scenario can be accounted for through constitutive relations for viscosity that depend on proppant concentration [1]. In the multi-phase approach, the granular phase and the carrier fluid are allowed to move separately [22,7]. Both single-phase and multi-phase approaches require the use of phenomenological constitutive equations to model the effect of particles in the slurry [12,17]. Generally, a constitutive model relates suspension stress to kinematics depending on particle concentration to take into account (1) suspension thickening and (2) particle contribution to suspension stress tensor [26]. To obtain constitutive relations, a combination of experimental work and computational modeling is necessary. The broad review of the constitutive modeling of dense suspensions was performed in [45].

The most recent and accurate semi-empirical constitutive relations for slurry were obtained in [8] and were used to study slurry flow in a channel using multi-phase methods [30,19]. Also, the accounting for the slip velocity between the phases in [19] allowed the transition between Poiseuille flow for clear fluid (or fluid with vanishingly small particle volume fractions) and Darcy filtration through the packed proppant (once the particle concentration reaches the packing limit).

Another relevant phenomenon in proppant transport is referred to as proppant bridging or tip screen-out [24,11,20,2]. Proppant bridging occurs when a proppant carried by the fracturing fluid creates a bridge of several particles across the fracture by blocking the flow of the slurry. This condition near the fracture tip results in the formation of a proppant pack that prevents the fracture from propagating. If this happens, an increase in pressure is required to continue the crack propagation – tip screen-out. Here we use a classical approach to account for bridging based on the assumption that the proppant bridges near the fracture tip when the fracture width divided by the proppant diameter becomes smaller than a prescribed amount, which is varied to simulate the effect of different bridging criteria and their influence on the solution.

The focus of this paper is to elucidate the effects of proppant on the near-front region of an HF propagating with a constant velocity without fluid lag. The problem is formulated for a slurry flow of proppant particles and a Newtonian fluid inside the fracture. We use a proppant transport model that accounts for the transition between Poiseuille flow for clear fluid and Darcy flow for highly concentrated proppant suspensions [19] and is based on the experimental work of [8]. The paper is organized as follows. Section 2 outlines the problem statement. Section 3 formulates the governing equations for the semi-infinite fracture with proppant slurry and the model for proppant transport. To calculate the numerical solution for the problem with proppant, we employ a non-singular formulation [16], which is adapted to the current problem and summarized in Section 4. Section 5 specifies limiting solutions for the HF without proppant to compare with the numerical results for the problem with proppant provided in Section 6. A summary and conclusions are discussed in Section 7.

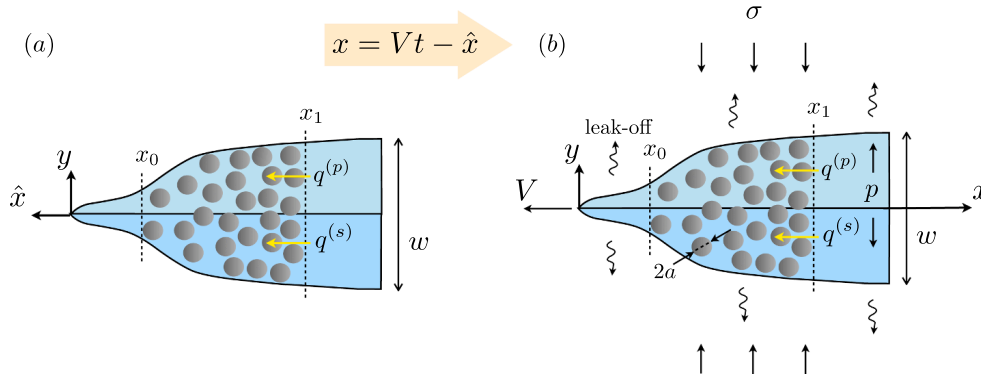


Fig. 1. Schematics of a plane strain hydraulic fracture (a) in the coordinate system (\hat{x}, y) and (b) in the moving coordinate system (x, y) , where V is a fracture propagation velocity. The fluid pressure inside the fracture is p and the far-field rock stress is σ . The proppant slurry occupies the region $x_0 < x < x_1$. The fluxes of proppant and slurry are denoted by $q^{(p)}$ and $q^{(s)}$, respectively.

2. Problem statement

The near-tip region of a hydraulic fracture is represented by a semi-infinite crack in a state of plane strain [40], as shown schematically in Fig. 1. Fig. 1a shows the fracture in the coordinate system (\hat{x}, y) centered at the tip. Crack propagation is accounted for by allowing the front to move with a constant velocity V . The problem is solved in the moving coordinate system (x, y) , in which the x coordinate is defined by: $x = Vt - \hat{x}$ (Fig. 1b). Note that the positive values of x lie inside the fracture (in the crack wake).

The fluid pressure p is introduced to open the HF by overcoming the uniform far-field rock stress σ that tends to resist crack opening displacements. We account for and define the fluxes of both the proppant and the slurry, $q^{(p)}$ and $q^{(s)}$, respectively. The slurry is assumed to be a mixture of Newtonian carrier fluid and spherical proppant particles of the same size. We assume the slurry flow in the domain $x \leq x_1$ and flow of clear Newtonian fluid at $x > x_1$. The boundary x_1 is determined by the proppant volume V_p . We account for proppant bridging which occurs when fracture opening is equal to several (N) particle diameters: $w = 2aN$, where a is proppant particle radius and N is referred to as bridging factor. The proppant bridging determines the boundary of the proppant region x_0 so that there is no proppant at $x < x_0$. In addition, Carter's model [10] is used to account for the fluid leak-off from the fracture surface into the rock formation. The mathematical problem is reduced to solving for the crack opening displacement (fracture opening) $w(x)$ and proppant concentration $\phi(x)$.

3. Governing equations

The equations governing the crack propagation include an elasticity equation, mass balance equations for proppant and slurry, and a fracture propagation criterion. To shorten mathematical expressions, all equations are cast in terms of the following scaled material parameters,

$$E' = \frac{E}{1 - \nu^2}, \quad K' = \sqrt{\frac{32}{\pi}} K_{Ic}, \quad \mu' = 12\mu, \quad C' = 2C_L, \quad (1)$$

where E and ν are Young's modulus and Poisson's ratio, K_{Ic} is the (rock) fracture toughness, μ is the intrinsic viscosity of the carrier Newtonian fluid, and C_L is Carter's leak-off coefficient.

3.1. Elasticity equation

The elasticity equation provides the relation between net pressure (difference between fluid pressure p and rock stress σ) and fracture opening w . The relation between the two is typically written so that the pressure is related to an integral involving the traction (in this case pressure) along the crack surfaces. Here we use the inverted form of that equation at constant σ [44,43,16],

$$w(x) = \frac{K'}{E'} x^{1/2} - \frac{4}{\pi E'} \int_0^\infty F(x, s) \frac{dp(s)}{ds} ds, \quad (2)$$

where the kernel of the above integral equation is defined as

$$F(x, s) = (s - x) \ln \left| \frac{x^{1/2} + s^{1/2}}{x^{1/2} - s^{1/2}} \right| - 2x^{1/2}s^{1/2}. \quad (3)$$

Formulating the elasticity problem in terms of Eq. (2) is preferable because it allows the determination of the fracture opening by direct substitution of the pressure gradient obtained from the lubrication equation. This, as discussed subsequently, makes it possible to circumvent numerical difficulties related to the pressure singularity along the crack front.

3.2. Fracture propagation criterion

The crack extends when the stress intensity factor is equal to the fracture toughness of the rock [27,41]. This criterion is enforced through the (near) crack tip relation between the stress intensity factor and the crack opening displacement,

$$w = \frac{K'}{E'} x^{1/2}, \quad x \rightarrow 0, \quad (4)$$

where K' is the scaled fracture toughness and E' is the scaled Young's modulus defined in Eq. (1). Note that elasticity Eq. (2) enforces propagation condition (4) in a corresponding limit, therefore Eq. (4) will not be directly used.

3.3. Slurry equations

The governing equations for the slurry flow follow from the proppant transport approach developed in [19,20] for the slurry flow of Newtonian fluid and proppant in a channel. The model is valid for the following assumptions: (1) low Reynolds number $Re \rightarrow 0$ (laminar flow), (2) high Peclet number $Pe \rightarrow \infty$ (purely hydrodynamic non-Brownian motion of particles).

Let ϕ define the average volume fraction of proppant across the fracture width. In this case, the governing mass balance equations can be written as

$$\text{Fluid: } \frac{\partial w(1-\phi)\rho^{(f)}}{\partial t} + \frac{\partial \rho^{(f)}q^{(f)}}{\partial \hat{x}} + \rho^{(f)}q_L = Q_0(1-\phi_0)\rho^{(f)}\delta(\hat{x}-\hat{x}_0), \quad (5a)$$

$$\text{Proppant: } \frac{\partial w\phi\rho^{(p)}}{\partial t} + \frac{\partial \rho^{(p)}q^{(p)}}{\partial \hat{x}} = Q_0\phi_0\rho^{(p)}\delta(\hat{x}-\hat{x}_0), \quad (5b)$$

where $\rho^{(f)}$ is the mass density of fluid, $\rho^{(p)}$ is the mass density of proppant, $q_L = C'/\sqrt{t-t_0(\hat{x})}$ corresponds to the volumetric flux of fluid leaking out of the fracture according to Carter's model [10], $t_0(\hat{x})$ is the time at which the crack tip was located at a point \hat{x} , ϕ_0 is a volume fraction of proppant at the injection, Q_0 is the injection rate, and the injection is assumed to be located at a point \hat{x}_0 . Recall that \hat{x} is the absolute spatial coordinate, which should not be confused with x , which is the coordinate relative to the moving crack tip. The system of mass balance Eq. (5) can be equivalently rewritten in a volumetric form by further assuming incompressibility of the fluid and particles as,

$$\text{Slurry: } \frac{\partial w}{\partial t} + \frac{\partial q^{(s)}}{\partial \hat{x}} + q_L = Q_0\delta(\hat{x}-\hat{x}_0), \quad (6a)$$

$$\text{Proppant: } \frac{\partial w\bar{\phi}}{\partial t} + \frac{\partial \bar{q}^{(p)}}{\partial \hat{x}} = \bar{\phi}_0 Q_0\delta(\hat{x}-\hat{x}_0), \quad (6b)$$

where the equation for slurry is obtained by summing the equations for fluid and proppant divided by the corresponding densities. The proppant equation is additionally normalized by the maximum packing volume fraction ϕ_m with $\bar{q}^{(p)} = q^{(p)}/\phi_m$ and $\bar{\phi} = \phi/\phi_m$ (so that $0 \leq \bar{\phi} \leq 1$). The maximum volume fraction $\phi_m = 0.585$ used in this work was estimated based on experimental observations in [8]. Note that this value depends on particle characteristics and is subject to debate, e.g. other experimental models proposed values of ϕ_m in the range of 0.603–0.68 [38]. The superscripts (f) , (p) , (s) correspond to fluid, proppant, and slurry, respectively. The slurry flux is given by $q^{(s)} = q^{(f)} + q^{(p)}$.

Mass balance equations for slurry (6a) and proppant (6b) can be further rewritten in a moving coordinate system associated with the fracture front as,

$$V \frac{dw}{dx} - \frac{dq^{(s)}}{dx} + C' \sqrt{\frac{V}{x}} = 0, \quad (7a)$$

$$V \frac{d(w\bar{\phi})}{dx} - \frac{d\bar{q}^{(p)}}{dx} = 0. \quad (7b)$$

Note that the last term in (7a) accounts for the fluid leak-off, the source terms are removed since they are not relevant for the semi-infinite fracture problem, and that steady-state conditions are assumed.

After integration of Eq. (7), the fluxes for slurry and proppant are obtained as,

$$q^{(s)} = wV + 2C'\sqrt{Vx}, \quad (8a)$$

$$\bar{q}^{(p)} = wV\bar{\phi}. \quad (8b)$$

To proceed, these expressions should be combined with the corresponding expressions coming from the proppant transport model, which are outlined next.

3.4. Proppant transport model

The relation between the flux and the pressure gradient is determined by the proppant transport model. In this paper, we use the semi-empirical constitutive relations obtained in [19] that are based on the experimental observations from [8]. In this framework, the volumetric fluxes for slurry and proppant are written as [19,20],

$$q^{(s)} = \frac{w^3}{\mu'} \hat{Q}^{(s)} \left(\bar{\phi}, \frac{w}{a} \right) \frac{dp}{dx}, \quad (9a)$$

$$\bar{q}^{(p)} = B \left(\frac{w}{a} \right) \hat{Q}^{(p)} \left(\bar{\phi}, \frac{w}{a} \right) q^{(s)}. \quad (9b)$$

Note that Eqs. (9) are written in a scalar form for the coordinate system shown in Fig. 1b where $\frac{dp}{dx} > 0$ and the fluxes $q^{(s)} > 0$, $\bar{q}^{(p)} > 0$. Unlike [19,20], in this paper we neglect proppant settling that would bring an additional term in Eq. (9b) for proppant flux. Neglecting proppant settling is a reasonable simplification for the near-tip region of the HF because the proppant reaches tight packing there. We do note that proppant settling is crucial for the general problem of a propagating hydraulic fracture.

In Eq. (9b), $B(w/a)$ denotes the blocking function,

$$B \left(\frac{w}{a} \right) = \frac{1}{2} H \left(\frac{w}{2a} - N \right) H \left(\frac{w_B - w}{2a} \right) \left[1 + \cos \left(\pi \frac{w_B - w}{2a} \right) \right] + H \left(\frac{w - w_B}{2a} \right), \quad (10)$$

that describes a smooth decrease of proppant flux near the fracture tip due to proppant bridging. The blocking function changes from $B = 0$ at $w < 2aN$ to $B = 1$ at $w > w_B = 2a(N + 1)$.

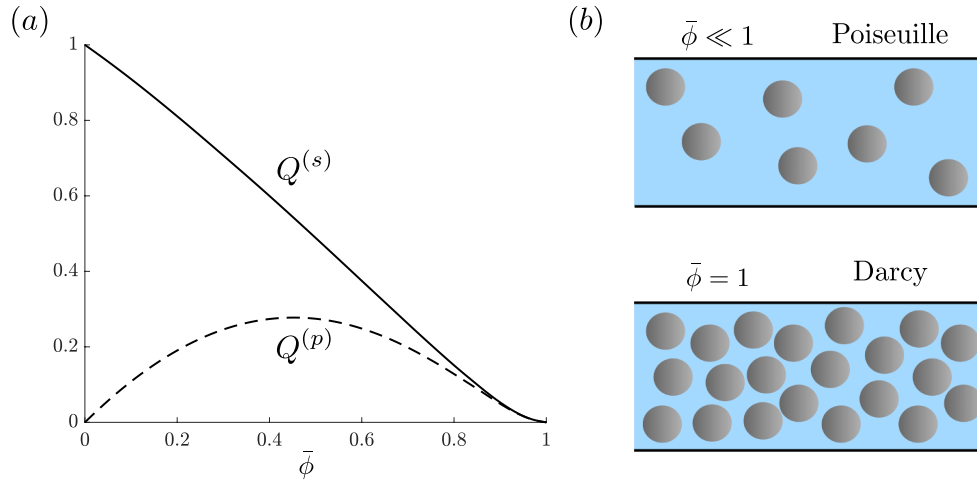


Fig. 2. (a) Variation of the suspension thickening function $Q^{(s)}$ and normalized proppant flux coefficient $Q^{(p)}$ vs the normalized proppant volume fraction [19]. (b) Schematics of the limiting regimes of slurry flow in a channel: Poiseuille flow at $\bar{\phi} \ll 1$ and Darcy filtration at $\bar{\phi} = 1$, which follows from the constitutive Eqs. (11).

The functions $\hat{Q}^{(s)}$ and $\hat{Q}^{(p)}$ have the following form,

$$\hat{Q}^{(s)} = Q^{(s)}(\bar{\phi}) + \frac{a^2}{w^2} \bar{\phi} D, \quad \hat{Q}^{(p)} = Q^{(p)}(\bar{\phi}) / \hat{Q}^{(s)}(\bar{\phi}, w/a), \quad (11)$$

where the dimensionless function $Q^{(s)}(\bar{\phi})$ describes suspension thickening with the addition of proppant and D is related to normalized permeability of the packed proppant. According to the developments in [19],

$$D = D_m = \frac{8(1 - \phi_m)^{\bar{\alpha}}}{3\phi_m} \text{ with } \bar{\alpha} = 4.1 \text{ and } \phi_m = 0.585. \quad (12)$$

The normalized permeability D_m is obtained on the basis of the hindered particle settling velocity correlation from [42], in which the limit of maximum particle concentration is taken. The functions $Q^{(s)}$, $Q^{(p)}$ have been computed numerically in [19] and are illustrated in Fig. 2a for completeness. The function $Q^{(s)}$ gradually decreases from one (for dilute suspension) to zero (for packing limit), while the function $Q^{(p)}$ initially increases linearly with proppant volume fraction, then saturates, and ultimately decreases to zero as the proppant approaches the packing concentration. To investigate the effect of the filtration term on the solution, we introduce the following quantity,

$$\mathcal{D} = \left(\frac{a^2}{w^2} \bar{\phi} D \right) / \hat{Q}^{(s)}, \quad (13)$$

which corresponds to the relative contribution of the Darcy filtration term into the slurry flux.

The adopted proppant transport model (9) accounts for the transition between Poiseuille flow for small proppant concentrations ($\bar{\phi} \ll 1$) to Darcy filtration for high concentrations ($\bar{\phi} \rightarrow 1$). Fig. 2b schematically shows channel flow for the corresponding limits. In the limit of zero proppant concentration ($\bar{\phi} = 0$), $Q^{(s)} = 1$ and $Q^{(p)} = 0$, and the Poiseuille flow of clear fluid is recovered,

$$q^{(s)} = \frac{w^3}{\mu'} \frac{dp}{dx}, \quad (14a)$$

$$\bar{q}^{(p)} = 0. \quad (14b)$$

In this work, we assume that there is no proppant at $x > x_1$, so suspension thickening function from Eq. (11) is equivalently written as,

$$\hat{Q}^{(s)} = \begin{cases} Q^{(s)}(\bar{\phi}) + \frac{a^2}{w^2} \bar{\phi} D, & x \leq x_1, \\ 1, & x > x_1. \end{cases} \quad (15)$$

In the limit of maximum proppant concentration ($\bar{\phi} = 1$), $Q^{(s)} = 0$ and $Q^{(p)} = 0$, and the equations for fluxes (9) are reduced to,

$$q^{(s)} = \frac{w\kappa'}{\mu'} \frac{dp}{dx}, \quad (16a)$$

$$\bar{q}^{(p)} = 0, \quad (16b)$$

which correspond to Darcy filtration of the carrier fluid through the packed proppant. Note that this Darcy limit is never reached in the considered model as we assume a non-zero slip velocity at the walls. In Eq. (16a), $\kappa' = Da^2$ is the scaled permeability of the packed proppant with the scaled permeability introduced as $\kappa' = 12\kappa$.

Permeability of the proppant pack κ can be related to the particle radius as [28,9,29],

$$\kappa = c_\kappa a^2, \quad (17)$$

where the value c_κ depends on the structure of the proppant packing [4]. It is instructive to estimate possible values of the dimensionless coefficient c_κ . At maximum proppant concentration $\phi_m = 0.585$, c_κ can be directly related to the coefficient $D = D_m$ given by Eq. (12),

$$D_m = 12c_\kappa, \quad (18)$$

which gives a permeability coefficient corresponding to the maximum proppant packing $c_\kappa \approx 10^{-2}$. The coefficient c_κ was also estimated for geometrically different types of packing in [4] as $6.5 \cdot 10^{-3}$ for cubic packing and $5.6 \cdot 10^{-3}$ for tetragonal packing of spheres. The Kozeny-Carman equation for the pressure drop through a packed bed of solids [28,9] when combined with Darcy equation gives the following relation,

$$c_\kappa = \frac{\Psi^2(1 - \phi)^3}{45\phi^2}, \quad (19)$$

where ϕ is a volume fraction of solids and Ψ is the particles' sphericity. For the maximum volume fraction $\phi = \phi_m = 0.585$ and sphericity of proppant $\Psi = 0.9$ (see for instance [33] for typical values of sphericity for ceramic proppants), Eq. (19) predicts $c_\kappa = 3.8 \cdot 10^{-3}$. Alternatively, based on the semi-empirical formula obtained in [37], the coefficient of permeability is written as,

$$c_\kappa = 0.204\phi^{4.58}, \quad (20)$$

which was obtained as best fits of the results for different particle shapes, including the pack of spherical particles with volume fraction $\phi = 0.4157$. For this volume fraction, according to (20), the following value is obtained $c_\kappa \approx 3.7 \cdot 10^{-3}$.

In this work, by default we use the value of $c_\kappa = D_m/12 \approx 10^{-2}$ ($D = D_m$). In addition, to take into account possible variability given the aforementioned estimations, we investigate sensitivity of the solution for smaller permeability using $c_\kappa = 10^{-3}$ ($D = 0.1 \cdot D_m$).

3.5. Fracture opening and proppant concentration equations

Eqs. (8) and (9) provide the expressions for fluxes from volume balance and slurry rheology points of view, respectively. Their combination leads to

$$\hat{Q}^{(s)}\left(\bar{\phi}, \frac{w}{a}\right) \frac{dp}{dx} = \left(V + 2C' \frac{\sqrt{Vx}}{w}\right) \frac{\mu'}{w^2}, \quad (21a)$$

$$B\left(\frac{w}{a}\right) \hat{Q}^{(p)}\left(\bar{\phi}, \frac{w}{a}\right) \frac{w^2}{\mu'} \hat{Q}^{(s)}\left(\bar{\phi}, \frac{w}{a}\right) \frac{dp}{dx} - V\bar{\phi} = 0. \quad (21b)$$

The pressure gradient is eliminated by combining Eqs. (21a) and (21b), to obtain the equation for proppant concentration $\bar{\phi}(w(x), x)$,

$$B\left(\frac{w}{a}\right) \hat{Q}^{(p)}\left(\bar{\phi}, \frac{w}{a}\right) \left(V + 2C' \frac{\sqrt{Vx}}{w}\right) - V\bar{\phi} = 0. \quad (22)$$

The corresponding relation for pressure gradient obtained from Eq. (21a) is of the form,

$$\frac{dp}{dx} = \left(V + 2C' \frac{\sqrt{Vx}}{w}\right) \frac{\mu'}{w^2} \frac{1}{\hat{Q}^{(s)}}. \quad (23)$$

This result is substituted into the elasticity Eq. (2) to obtain the integral equation for the fracture width as,

$$w(x) = \frac{K'}{E'} x^{1/2} - \frac{4\mu'}{\pi E'} \int_0^\infty F(x, s) \left(V + 2C' \frac{\sqrt{Vs}}{w(s)}\right) \frac{1}{w^2(s) \hat{Q}^{(s)}} ds, \quad (24)$$

with $\hat{Q}^{(s)}$ given by Eq. (15) and for the purpose of numerical calculations substituted using the Heaviside step function $H(x - x_1)$. The proppant boundary x_1 is determined by the finite proppant volume V_p and the additional proppant volume equation is specified in Section 3.6. The system of Eqs. (22), (24) can be solved to obtain proppant concentration $\bar{\phi}(x)$ and fracture opening $w(x)$ without the need to compute the pressure field. However, for completeness of numerical results, pressure is calculated as well from lubrication Eq. (23),

$$p(x) = \sigma - \int_x^\infty \left(V + 2C' \frac{\sqrt{Vx}}{w}\right) \frac{\mu'}{w^2} \frac{1}{\hat{Q}^{(s)}} dx, \quad (25)$$

where the fact that the net pressure ($p - \sigma$) vanishes at infinity is used. Since σ is assumed to be constant, from here on we assume that $\sigma = 0$ without loss of generality.

3.6. Proppant volume equation

The fracture is semi-infinite in length, but we consider the case of finite proppant volume, V_p , which occupies the region $[x_0, x_1]$. Location of the boundary x_0 (closer to the tip) is governed by proppant bridging. This boundary can be determined from numerical solution of the concentration Eq. (22) under the following condition: $\bar{\phi}(x < x_0) = 0$. The other boundary x_1 is determined by the total proppant volume V_p ,

$$V_p = \int_{x_0}^{x_1} w(x) \phi_m \bar{\phi}(x) dx, \quad (26)$$

or, taking into account that $\bar{\phi}(x < x_0) = 0$, equivalently,

$$V_p = \int_0^{x_1} w(x) \phi_m \bar{\phi}(x) dx. \quad (27)$$

Note that $\bar{\phi}(x)$ vanishes for $x < x_0$ due to bridging and it is assumed that there is no proppant behind the packed region. The latter assumption can be relaxed if necessary.

In summary, the system of the governing equations consists of (22), (24), and (27) to obtain fracture opening $w(x)$ and proppant concentration $\bar{\phi}(x)$ depending on distance from the tip, as well as proppant boundaries x_0 and x_1 (where x_0 comes naturally from the solution for $\bar{\phi}(x)$).

4. Scaled form of governing equations

In this section, the governing equations are written using a non-singular formulation similar to [16,18,6]. To decrease the number of unknowns and to be consistent with previous works, the equations are formulated in terms of the following dimensionless quantities,

$$\begin{aligned} \tilde{w} &= \frac{wE'}{K'\chi^{1/2}}, \quad \tilde{x} = \left(\frac{x}{l}\right)^{1/2}, \quad \tilde{s} = \left(\frac{s}{l}\right)^{1/2}, \quad \tilde{x}_0 = \left(\frac{x_0}{l}\right)^{1/2}, \quad \tilde{x}_1 = \left(\frac{x_1}{l}\right)^{1/2}, \quad l = \left(\frac{K'^3}{\mu'VE'^2}\right)^{1/2}, \quad \chi = \frac{2C'E'}{V^{1/2}K'}, \\ \tilde{a} &= \frac{aE'}{K'l^{1/2}} = \frac{aE'^3\mu'V}{K'^4}, \quad \tilde{V}_p = \frac{V_pE'}{2K'l^{3/2}} = \frac{V_pE'^7\mu'^3V^3}{2K'^{10}}, \end{aligned} \quad (28)$$

where the scaled parameters are referred to as follows: \tilde{w} is fracture width, \tilde{x} is the distance from the crack tip, \tilde{s} is the variable of integration, $[\tilde{x}_0, \tilde{x}_1]$ are the proppant boundaries, l is the length scale, χ is the leak-off parameter, \tilde{a} is the proppant radius, and \tilde{V}_p is the proppant volume. Note that parameters \tilde{a} , and \tilde{V}_p are associated with proppant characteristics but also depend on the fracture propagation velocity V and material properties of the rock and the fluid.

Elasticity Eq. (24) is rewritten using the scaled parameters (28) as

$$\tilde{w}(\tilde{x}) = 1 + \frac{8}{\pi} \int_0^\infty G\left(\frac{\tilde{s}}{\tilde{x}}\right) \left(\frac{1}{\tilde{w}(\tilde{s})^2} + \frac{\chi}{\tilde{w}(\tilde{s})^3} \right) \frac{1}{\hat{Q}(\tilde{s})} d\tilde{s}, \quad (29)$$

where the integral kernel

$$G(t) = \frac{1-t^2}{t} \ln \left| \frac{1+t}{1-t} \right| + 2 \quad (30)$$

is not singular and $0 \leq G(t) \leq 4$. Note that in this formulation $\tilde{w} \geq 1$. The inverse viscosity coefficient (15) is written in terms of the scaled quantities (28) as

$$\hat{Q}(\tilde{s}) = \begin{cases} Q^{(s)}(\bar{\phi}) + \left(\frac{\tilde{a}}{\tilde{w}\tilde{x}}\right)^2 \bar{\phi} D, & \tilde{x} \leq \tilde{x}_1, \\ 1, & \tilde{x} > \tilde{x}_1. \end{cases} \quad (31)$$

The fracture propagation criterion (4),

$$\tilde{w} = 1, \quad \tilde{x} \rightarrow 0, \quad (32)$$

is automatically satisfied from Eq. (29).

The concentration Eq. (22) is written as

$$B\hat{Q}^{(p)} \left(1 + \frac{\chi}{\tilde{w}} \right) - \bar{\phi} = 0, \quad (33)$$

where $\hat{Q}^{(p)} = Q^{(p)}/\hat{Q}^{(s)}$ and the blocking function (10) is rewritten as

$$B = \frac{1}{2} H \left(\frac{\tilde{w}\tilde{x}}{2\tilde{a}} - N \right) H \left((N+1) - \frac{\tilde{w}\tilde{x}}{2\tilde{a}} \right) \left[1 + \cos \left(\pi \left[(N+1) - \frac{\tilde{w}\tilde{x}}{2\tilde{a}} \right] \right) \right] + H \left(\frac{\tilde{w}\tilde{x}}{2\tilde{a}} - (N+1) \right). \quad (34)$$

The equation for fluid pressure (25) at $\sigma = 0$ has the following scaled form,

$$\Pi(\tilde{x}) = - \int_{\tilde{x}}^{\infty} \frac{2}{\tilde{w}^2 \tilde{x}} \left(1 + \frac{\chi}{\tilde{w}} \right) \frac{1}{\hat{Q}^{(s)}} d\tilde{x}, \quad (35)$$

where the dimensionless variable for scaled pressure is introduced as

$$\Pi = p \frac{K' V^2}{\mu' E' V}. \quad (36)$$

The proppant volume Eq. (27) is written as follows,

$$\tilde{V}_p = \phi_m \int_0^{\tilde{x}_1} \tilde{w}(\tilde{x}) \tilde{x}^2 \tilde{\phi}(\tilde{x}) d\tilde{x}. \quad (37)$$

The resultant system of Eqs. (29), (33), and (37) is solved numerically to obtain \tilde{w} , $\tilde{\phi}$, and \tilde{x}_1 .

5. Asymptotic solutions for fracture opening

It is useful to compare the effects of proppant on the different regimes of fracture propagation with those associated with the limiting solutions for the semi-infinite hydraulic fracture problem without proppant. For a Newtonian fluid, there are three such limiting (asymptotic) solutions,

$$w_k = \frac{K'}{E'} x^{1/2}, \quad w_{\tilde{m}} = \beta_{\tilde{m}} \left(\frac{4\mu'^2 V C'^2}{E'^2} \right)^{1/8} x^{5/8}, \quad w_m = \beta_m \left(\frac{\mu' V}{E'} \right)^{1/3} x^{2/3}, \quad (38)$$

where $\beta_{\tilde{m}} = 4/(15^{0.25}(\sqrt{2} - 1)^{0.25})$ and $\beta_m = 2^{1/3} 3^{5/6}$ are constants. Here w_k denotes the fracture opening solution for the “dry” or toughness dominated fracture [41], $w_{\tilde{m}}$ is the solution for the leak-off dominated regime [32], and w_m is the solution for the viscosity dominated regime [13]. The asymptotic solutions (38) can be rewritten in a scaled form using Eq. (28) as follows,

$$\tilde{w}_k = 1, \quad \tilde{w}_{\tilde{m}} = \beta_{\tilde{m}} \chi^{1/4} \tilde{x}^{1/4}, \quad \tilde{w}_m = \beta_m \tilde{x}^{1/3}. \quad (39)$$

6. Numerical results

Integral Eq. (29), the concentration Eq. (33) and the proppant volume Eq. (37) are solved simultaneously for three unknowns: $\tilde{w}(\tilde{x})$, $\tilde{\phi}(\tilde{x})$, \tilde{x}_1 . First, integral in (29) is discretized using Simpson’s rule. Then, the discretized Eq. (29) is solved using Newton’s method with an initial guess for \tilde{x}_1 and with an initial guess for \tilde{w} corresponding to a solution without proppant. At each iteration, the proppant concentration $\tilde{\phi}(\tilde{x})$ and the proppant boundary \tilde{x}_1 are recalculated using the updated \tilde{w} . The proppant concentration $\tilde{\phi}(\tilde{x})$ is restricted to $0 \leq \tilde{\phi} < 1$ and is obtained solving Eq. (33) using bisection method. The proppant boundary \tilde{x}_1 is calculated for updated \tilde{w} and $\tilde{\phi}$ from the proppant volume Eq. (37) using Matlab “fsolve()” function. The process is repeated until convergence is attained.

The solution depends on the following parameters: the proppant pack permeability for a tight packing D , the number of proppant particles resulting in proppant bridging N , and the dimensionless parameters related to leak-off χ , the proppant radius \tilde{a} , the proppant volume \tilde{V}_p , and the distance from the tip \tilde{x} . In the calculations, we use the maximum proppant concentration $\phi_m = 0.585$ [8], while to account for a possible variation of normalized permeability D (Eq. (12)) based on physical estimates from Section 3.4, we consider two cases $D = D_m$ and $D = 0.1 \cdot D_m$ in some calculations. The number of proppant particles resulting in proppant bridging $N = 3$ is used [15] in most of the calculations by default. To account for sensitivity to bridging factor, its variation from $N = 1$ to $N = 3$ is used for some cases to cover the range generally used in hydraulic fracturing simulations [14].

It is instructive to first estimate the range of dimensionless parameters that influence the solution. To this end, let the physical properties be: $K_{Ic} = 1$ MPa·m^{0.5}, $E = 30$ GPa, $\nu = 0.2$, $1 \leq \mu \leq 5$ cP, $10^{-3} \leq V_p \leq 1$ m², $0.05 \leq a \leq 1.19$ mm, $5 \cdot 10^{-8} \leq C_L \leq 10^{-3}$ m/s^{0.5}, $0.001 \leq V \leq 0.25$ m/s, and $x = 10$ m. Some values are taken constant and some are given ranges to capture variation of the parameters. With the help of Eq. (1) and Eq. (28), these parameters yield the variation of the scaled parameters in the following ranges, approximately: \tilde{a} from 10^{-4} to 1, \tilde{V}_p from 10^{-10} to 10^3 , χ from 10^{-2} to 10^3 , and \tilde{x} from 10^{-3} to 3.

However, since both parameters \tilde{a} and \tilde{V}_p additionally depend on the same properties of fluid and rock, not every combination of the aforementioned \tilde{a} and \tilde{V}_p is physically meaningful. Fig. 3 outlines a region in the parameter space of \tilde{a} and \tilde{V}_p obtained based on the variation of the problem parameters a , V_p , μ , and V , as discussed above. The point shown inside the parameter space as an example corresponds to the following set of physical parameters: $\mu = 1$ cP, $V_p = 4 \cdot 10^{-2}$ m², $a = 0.4$ mm, $V = 1$ cm/s. Arrows show the directions in which a point inside the parameter space moves with a change of a particular parameter. Fluid viscosity μ and propagation velocity V appear in both expressions for \tilde{a} and \tilde{V}_p given by Eq. (28) as a product, therefore they shift a point in the parameter space along the same direction. Results demonstrate that the admissible values of the dimensionless particle size and volume are related and occupy a relatively narrow band. Therefore, care should be taken when varying these parameters simultaneously. Most of the numerical results will be shown in terms of the scaled properties to cover the range of values shown in the Fig. 3 and the different values of leak-off parameter χ .

6.1. Proppant solution in parameter space

To show the effect of proppant on the fracture tip region in parameter space, Fig. 4 shows a variation of the scaled fracture width

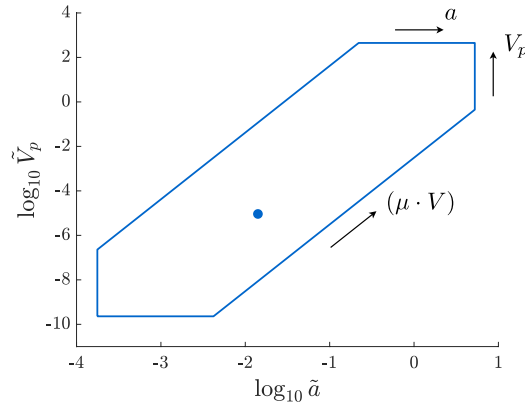


Fig. 3. Parameter space for the admissible values of \tilde{a} and \tilde{V}_p (outlined) based on variation of the following physical parameters: proppant volume V_p , particle radius a , fluid viscosity μ , and fracture propagation velocity V . The point corresponds to $\mu = 1$ cP, $V_p = 4 \cdot 10^{-2} \text{ m}^2$, $a = 0.4$ mm, $V = 1$ cm/s.

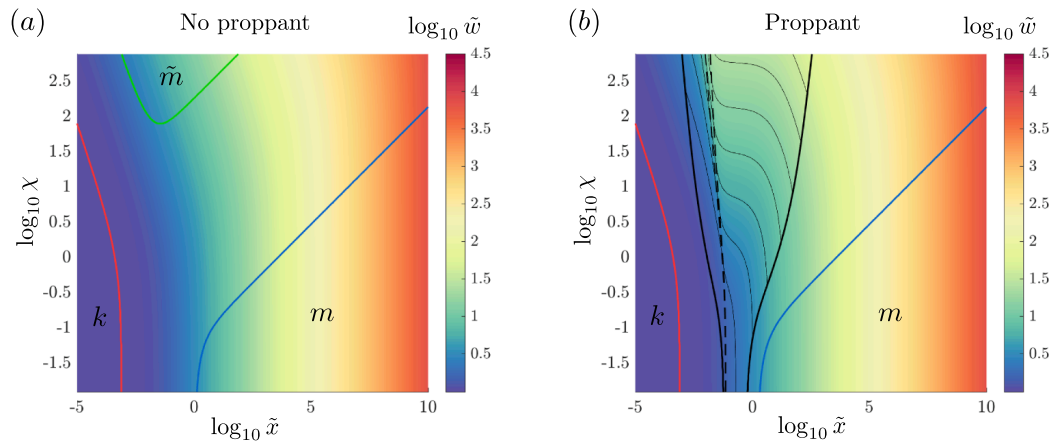


Fig. 4. Numerical solution for the scaled fracture opening \tilde{w} versus scaled distance from the tip \tilde{x} and leak-off χ : (a) without proppant and (b) with proppant. Dashed lines in (b) show the location of proppant. Thick black solid lines outline the region with \tilde{w} affected by proppant by more than 1%. Thin black lines are the contour lines of \tilde{w} . Red, green, and blue lines outline the regions of the toughness (k), the leak-off (\tilde{m}), and the viscosity (m) limiting solutions, respectively, Eq. (39). (For interpretation of the references to colour in this figure legend, the reader is referred to the web version of this article.)

\tilde{w} versus dimensionless leak-off χ and coordinate \tilde{x} : without proppant (a) and in the presence of proppant (b). The solution with proppant was obtained for the following parameters: $\tilde{a} \approx 1.41 \cdot 10^{-2}$, $\tilde{V}_p \approx 9.17 \cdot 10^{-6}$, $D = D_m$, and $N = 3$ which corresponds to the point illustrated in a parameter space in Fig. 3. Solution without proppant shown in Fig. 4a agrees with previously obtained results in [16]. The red, green, and blue lines outline the zones within which the relative difference between the numerical solution \tilde{w} and toughness (k), leak-off (\tilde{m}), and viscosity (m) limiting solutions Eq. (39) is below 1%. Fig. 4b shows the numerical solution for the problem with proppant in similar parameter space. Dashed lines show the proppant region boundaries, while thick black lines outline the region where the solution with proppant differs from the corresponding solution without proppant by more than 1%. The latter region extends far beyond the zone of the physical location of proppant and the fracture width is significantly increased in this region. To highlight the effect of proppant on the fracture width, thin solid black contour lines in Fig. 4b are added to indicate constant levels of \tilde{w} . Scaled fracture width has a steep increase near the proppant pack and remains approximately constant in a wide region behind it. This nearly “plateau” behavior behind the proppant pack ($\tilde{w} \approx \text{constant}$) can be interpreted as a toughness dominated solution with an effective increased fracture toughness K'_{eff} ($\tilde{w} = K'_{\text{eff}}/K'$). The “plateau” behavior of the scaled fracture width $\tilde{w} = \text{constant}$ corresponds to the square root behavior $w \propto x^{1/2}$ in terms of unscaled variables.

Outside of the region affected by proppant, the numerical solution approaches the solution without proppant with its limiting asymptotic solutions. For the considered set of scaled parameters, the toughness dominated regime appears in the same region for both solutions with and without proppant, while the viscosity dominated regime is slightly shifted farther from the tip for the solution with proppant. The leak-off dominated regime visually disappears from the diagram in Fig. 4b because the proppant influence zone completely covers it. This is a result of the adopted set of problem parameters, and, for some other parameter sets, leak-off dominated region may be partially visible. Note that the region affected by proppant appears to be localized only on a logarithmic scale and, for typical fracture lengths, a transition to the solution without proppant may not be reached.

6.2. Proppant radius and volume

To investigate the influence of dimensionless particle radius \tilde{a} , Fig. 5 shows the scaled fracture width \tilde{w} versus \tilde{x} for the fixed values of leak-off χ and different values of \tilde{a} . Fig. 5a corresponds to the small leak-off case ($\chi = 10^{-2}$) and Fig. 5b corresponds to the large leak-off case ($\chi = 10^2$). Solid gray lines indicate the solution without proppant, which differs from the solution with proppant in localized regions that are affected by the proppant pack. Solid black lines indicate solution with proppant calculated using the following parameters: $\tilde{a} = \{10^{-4}, 10^{-3}, 10^{-2}\}$ and $\tilde{V}_p = 10^{-5}$. The computed boundaries of the proppant pack \tilde{x}_0 and \tilde{x}_1 are indicated by the hollow and filled black circles, respectively. For the small leak-off case, the solution is bounded from below by the toughness (red dashed line) and the viscosity (blue dashed line) asymptotes (39). For the large leak-off case, the solution is bounded from below by an additional leak-off asymptote (green dashed line) (39) and the fracture width in this region increases making the fracture tip sharper. For a fixed \tilde{x} , the increase in fracture opening caused by proppant is noticeably larger for the large leak-off case. This is explained by noting that the condition of fixed \tilde{x} and fixed distance from the tip x results in a fixed fracture front propagation velocity V according to Eq. (28). Physically, to keep the velocities of fracture fronts for large and small leak-off equal, a fluid loss into the rock for the large leak-off case must be compensated by a higher velocity of fluid inside the fracture. This higher fluid velocity is associated with a larger pressure gradient and explains a larger fracture opening for the large leak-off case.

The arrow in Fig. 5 indicates the direction in which solutions shift as \tilde{a} increases. For the same proppant volume, proppant with a smaller radius has a larger influence on the fracture opening behind the proppant pack. Physically, there are two contributing factors. First, proppant with smaller size packs closer to the fracture tip following the bridging criterion. As a result, the fracture widens as compared to a larger proppant size. Second, smaller particles form tighter proppant packing with smaller permeability, leading to a decreased fracture conductivity which causes a larger pressure jump over the proppant pack making the fracture wider. It is also interesting to observe the ‘‘plateau’’ behavior behind the proppant pack, which was described above for Fig. 4.

To show the effect of proppant volume, the numerical solution for $\tilde{V}_p = \{10^{-4}, 10^{-3}, 10^{-2}\}$ and $\tilde{a} = 10^{-2}$ is shown in Fig. 6. Fig. 6a shows the solution for the small leak-off case and Fig. 6b corresponds to the large leak-off case. Note that Fig. 6 uses the same notations as Fig. 5. As can be seen from the results, the effect of proppant increases with proppant volume. The qualitative behavior of the solution is similar to that shown in Fig. 5. Besides, in contrast to Fig. 5, the left boundary of the proppant is not significantly affected by \tilde{V}_p since proppant volume does not influence the selected bridging criterion. At the same time, the right boundary of the proppant pack shifts away from the tip as the proppant volume increases.

Next, we show the expanded numerical results that include fracture opening, proppant concentration, pressure profile, and additionally calculated filtration term. Note that for all the following figures, the green, red, and blue colors are not related to leak-off, toughness, and viscosity asymptotic solutions unless mentioned specifically. Figs. 7, 8 show the numerical results depending on \tilde{a} and \tilde{V}_p , respectively, for the same parameters as in Figs. 5, 6 but for only one value of leak-off. As an example, let us show the dependence on \tilde{a} for the large leak-off $\chi = 10^2$ and the dependence on \tilde{V}_p for the small leak-off $\chi = 10^{-2}$. To demonstrate the effect of proppant on the fracture shape near the fracture tip, we plot $\Omega = \tilde{w}\tilde{x} \propto w$ versus $\xi = \tilde{x}^2 \propto x$ that gives fracture shape in relative units. In Fig. 7a, that shows fracture opening Ω , the range for ξ is chosen to illustrate the proppant region and the region immediately behind it which are the most relevant for the analysis. In these regions, the presence of proppant significantly increases fracture opening (colored lines) as compared to the solution without proppant (gray line). For smaller values of \tilde{a} , the effect is larger. In contrast to Fig. 7a, Figs. 7b-d show the results on a logarithmic scale.

Fig. 7b shows the relative contribution of Darcy filtration which is non-zero only in a region with proppant, as expected. The filtration \mathcal{D} has a peak near the boundary closest to the tip, while, along the pack of proppant, \mathcal{D} decreases with distance from the tip. The peak values at the onset of the proppant pack $\mathcal{D} > 0.93$ are close to the Darcy filtration limit ($\mathcal{D} = 1$) which suggests that

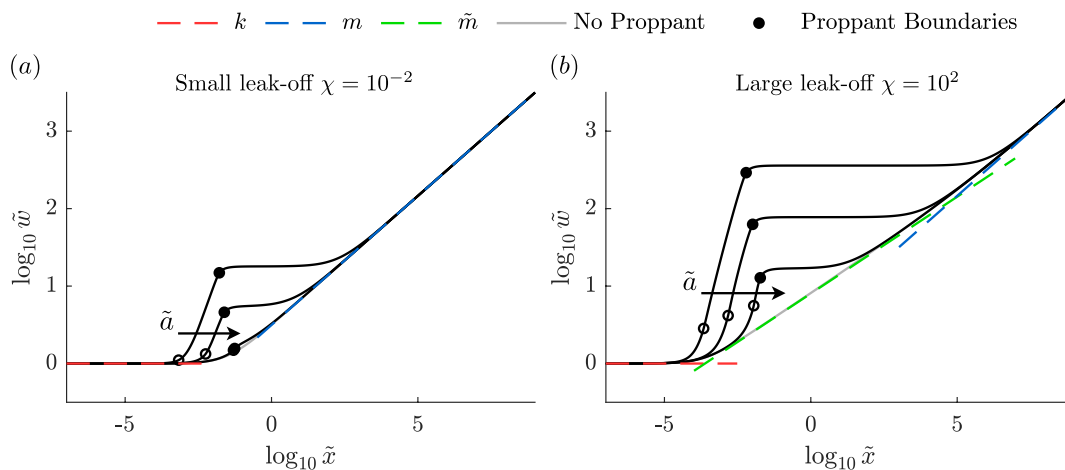


Fig. 5. The scaled fracture opening \tilde{w} versus \tilde{x} for different values of the scaled proppant radius $\tilde{a} = \{10^{-4}, 10^{-3}, 10^{-2}\}$ and $\tilde{V}_p = 10^{-5}$ (black lines) for (a) small and (b) large leak-off. The red, green, and blue dashed lines correspond to k , \tilde{m} , m limiting solutions (39). The gray lines show a solution without proppant. The proppant region boundaries are indicated by circles. (For interpretation of the references to colour in this figure legend, the reader is referred to the web version of this article.)

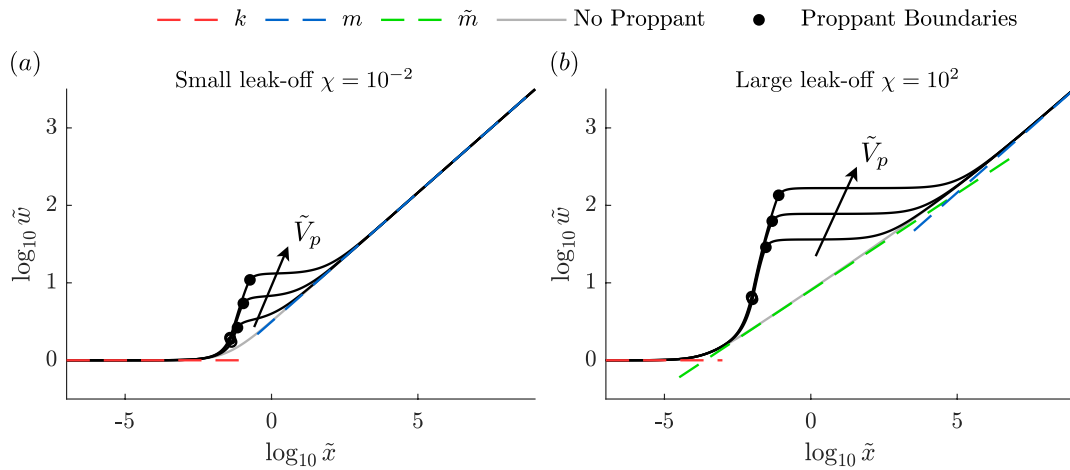


Fig. 6. The scaled fracture opening \tilde{w} versus \tilde{x} for different values of scaled proppant volume $\tilde{V}_p = \{10^{-4}, 10^{-3}, 10^{-2}\}$ and $\tilde{a} = 10^{-2}$ (black lines) for (a) small and (b) large leak-off. The red, green, and blue dashed lines correspond to k , \tilde{m} , m solutions (39). The gray lines show a solution without proppant. The proppant region boundaries are indicated by circles. (For interpretation of the references to colour in this figure legend, the reader is referred to the web version of this article.)

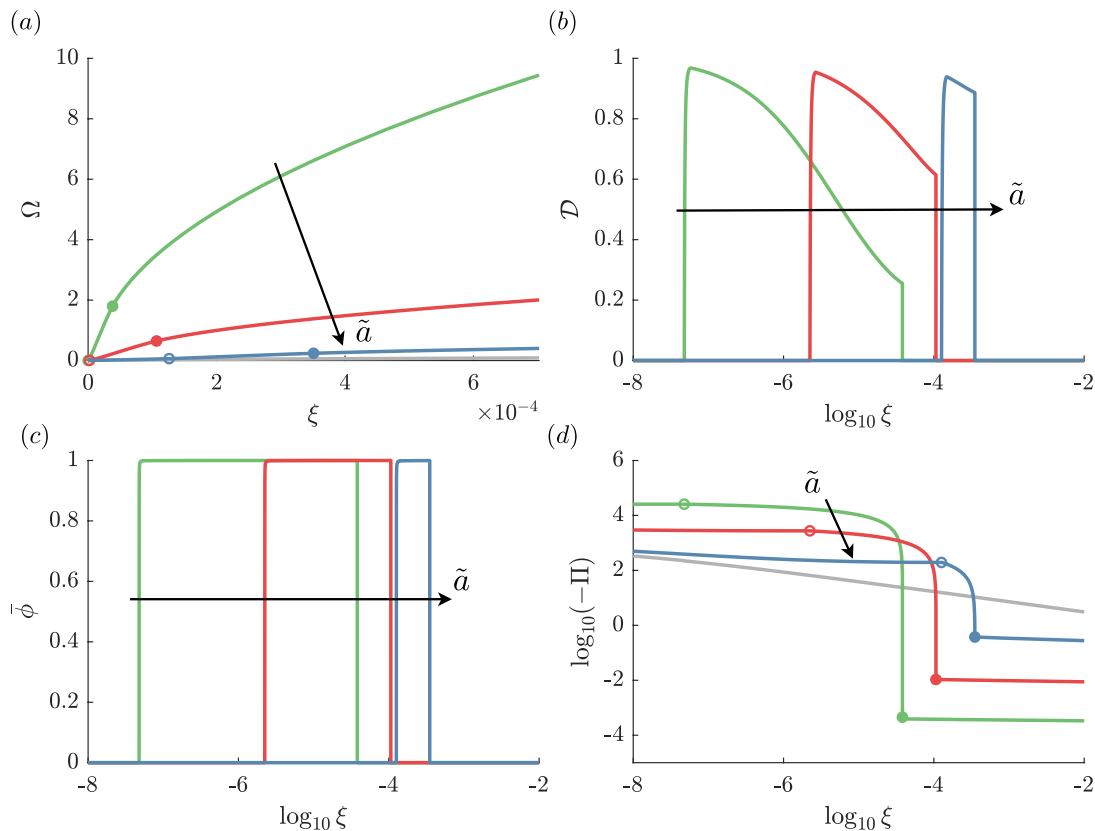


Fig. 7. Sensitivity to scaled proppant radius $\tilde{a} = \{10^{-4}, 10^{-3}, 10^{-2}\}$ at $\tilde{V}_p = 1 \cdot 10^{-5}$ and large leak-off $\chi = 10^2$. Numerical solution for (a) scaled fracture opening, (b) relative effect of Darcy filtration, (c) proppant concentration, and (d) fluid pressure. The proppant region boundaries are indicated by circles. Gray lines in (a), (d) show the solution without proppant.

filtration almost dominates the response. For different \tilde{a} , the effect of Darcy filtration in Fig. 7b is similar and the difference for various \tilde{a} is mostly due to a different location of the proppant pack. Fig. 7c shows that on a logarithmic scale, the location of the proppant pack shifts away from the crack tip as \tilde{a} (or proppant particle size) increases which is consistent with the bridging criterion incorporated via the blocking function. The proppant approaches tight packing with the maximum allowable concentration ($\tilde{\phi} \rightarrow 1$) throughout the whole pack which contributes to the high effect of filtration. This behavior characterizes the large leak-off case while for the small leak-off case the maximum allowable concentration is reached farther from the tip which dramatically decreases the effect of filtration \mathcal{D} as it will be discussed in Section 6.3.

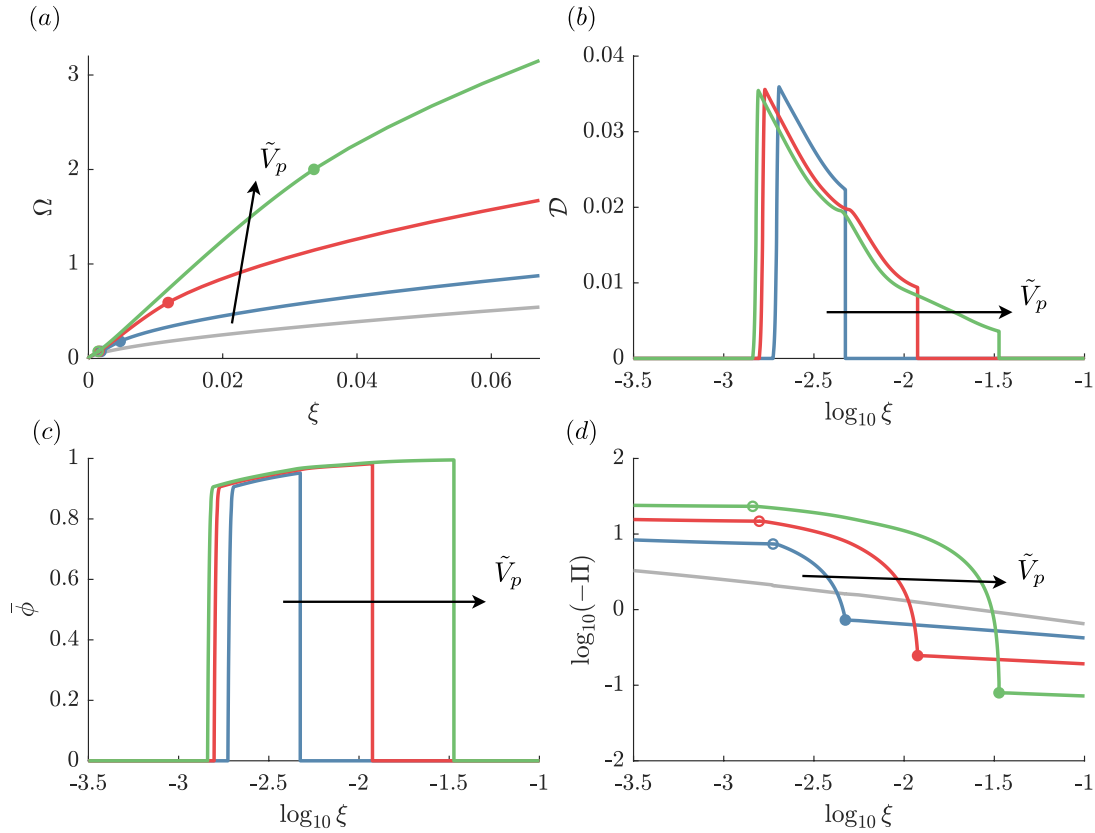


Fig. 8. Sensitivity to scaled proppant volume $\tilde{V}_p = \{10^{-4}, 10^{-3}, 10^{-2}\}$ at $\tilde{a} = 1 \cdot 10^{-2}$ and small leak-off $\chi = 10^{-2}$. Numerical solution for (a) scaled fracture opening, (b) relative effect of Darcy filtration, (c) proppant concentration, and (d) - pressure. The proppant region boundaries are indicated by circles. Gray lines in (a), (d) show the solution without proppant.

Fig. 7d illustrates a pressure profile in relative units. The vertical axis corresponds to the logarithm of a negative pressure. The solutions with (colored lines) and without proppant (gray line) follow the same behavior far from the tip and close to the tip, while Fig. 7d specifically shows the region near the proppant pack where the proppant solution significantly deviates from the solution without proppant. Proppant increases pressure right behind the proppant pack and decreases it in front of it, i.e., close to the fracture tip (colored lines). Pressure jump over the proppant region decreases with the increase of particle size because of the increased permeability of the packed proppant (and fracture conductivity) at large \tilde{a} .

The effects of proppant volume \tilde{V}_p on the expanded numerical results are illustrated for the small leak-off case in Fig. 8. Fig. 8a shows that the fracture opening Ω increases with the proppant volume at the length scale of the proppant pack location. The proppant sharpens the crack opening profile near the tip. Fig. 8b shows that, for the small leak-off case, the peak values of \mathcal{D} are significantly less than the Darcy limit which means that the effect of filtration is insignificant and the flow follows Poiseuille equation with a viscosity increased due to proppant. Normalized proppant concentration, in this case, has a jump at the left boundary of proppant and then slowly increases approaching the concentration limit $\phi \rightarrow 1$ farther from the tip (Fig. 8c). Fig. 8d similarly to Fig. 7d shows a pressure profile without proppant (gray line) and with proppant (colored lines). For the solution with proppant, increasing \tilde{V}_p shifts the right boundary of the pack farther away from the tip and also increases a pressure jump over the proppant pack.

6.3. Proppant pack permeability

The distribution of packed proppant can change permeability significantly (up to one order based on estimates of different models). In turn, this variation of permeability affects the numerical solution for the near-tip region of the fracture. To investigate this effect, in Fig. 9, we compare the numerical solutions for $D = 0.1 \cdot D_m$ (red lines) and D_m (blue lines) which correspond to $c_x = 10^{-3}$ and $c_x = 10^{-2}$, respectively. Here D_m is given by Eq. (12) and c_x is the coefficient relating permeability to squared particle radius from Eq. (17) and its estimates are discussed in Section 3.4. Fig. 9 shows the results for both small (dashed lines) and large leak-off (solid lines) at $\tilde{a} = 1 \cdot 10^{-2}$, $\tilde{V}_p = 1 \cdot 10^{-4}$, and $N = 3$. The solutions without proppant were excluded from Fig. 9 to improve readability but they were previously shown in Figs. 7, 8 for large and small leak-off, respectively.

The increase of permeability decreases fracture opening (Fig. 9a) as a result of the lower pressure jump over the packed region (Fig. 9d). This causes the proppant pack to shift away from the fracture tip. The filtration \mathcal{D} is significantly affected by leak-off (Fig. 9b). For the small leak-off case, \mathcal{D} is not larger than 0.04, while for the large leak-off case the peak value of \mathcal{D} is larger than 0.9 and is reached near the left boundary of the packed proppant. This results from slurry dehydration which occurs rapidly for the large

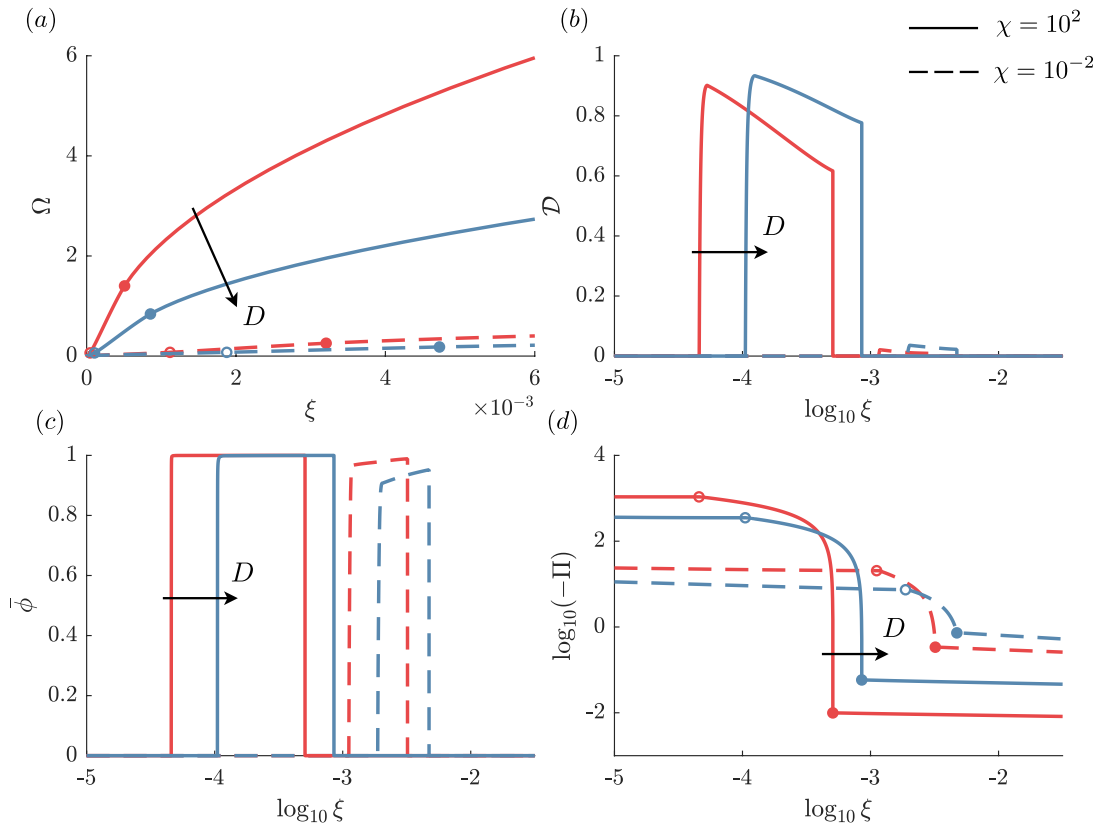


Fig. 9. Sensitivity to proppant pack permeability $D = \{0.1 \cdot D_m, D_m\}$ at small ($\chi = 10^{-2}$, dashed lines) and large ($\chi = 10^2$, solid lines) leak-off. Numerical solution for (a) scaled fracture opening, (b) relative effect of Darcy filtration, (c) proppant concentration, and (d) pressure at $\tilde{a} = 1.10^{-2}$, $\tilde{V}_p = 1.10^{-4}$. The proppant region boundaries are indicated by circles.

leak-off case, accelerating the formation of the proppant pack with a nearly maximum concentration of proppant, $\bar{\phi} \rightarrow 1$, near the crack tip (solid lines, Fig. 9c). Alternatively, for the small leak-off cases, the proppant concentration near the left boundary of the proppant pack is less than the maximum value and the concentration limit is approached farther from the tip (dashed lines, Fig. 9c). This decreases proppant filtration \mathcal{D} (dashed lines, Fig. 9b) and fracture opening (dashed lines, Fig. 9a) as compared to the large leak-off case. Moreover, it is observed that \mathcal{D} decreases with distance from the tip even when the proppant concentration approaches 1 next to the right boundary of the proppant pack. This suggests that it is not the proppant concentration that determines the decay of \mathcal{D} but the fracture opening which increases with distance from the fracture front, or mathematically,

$$\mathcal{D} = 1 / \left(1 + \left(\frac{w}{a} \right)^2 \frac{Q^s(\bar{\phi})}{\bar{\phi} D} \right), \tag{40}$$

which comes from Eq. (13) using Eq. (15) at $x \leq x_1$. This relation also explains that the maximum of \mathcal{D} slightly increases with pack permeability D (Fig. 9b) as a result of both the increase in the parameter D itself and the decrease in fracture opening w .

6.4. Proppant bridging

In this section, we investigate the influence of different bridging criteria, which are constructed by varying the bridging factor N in the blocking function Eq. (34). As in hydraulic fracturing applications a bridging factor is typically varied in a range $N = 1-3$, we compare the solutions for $N = 1$ and $N = 3$.

Fig. 10 illustrates the relative difference $(\tilde{w}_{N=1} - \tilde{w}_{N=3}) / \tilde{w}_{N=1}$ for the following set of parameters: $\tilde{a} \approx 1.41 \cdot 10^{-2}$, $\tilde{V}_p \approx 9.17 \cdot 10^{-6}$, $D = D_m$. The corresponding solution for the same parameter set with $N = 3$, $w_{N=3}$, was shown in Fig. 4, and with $N = 1$, $\tilde{w}_{N=1}$, was additionally calculated. Fig. 10a shows the relative difference between the two for the whole range of χ and \tilde{x} . Red and blue lines (Fig. 10a) outline the regions where \tilde{w} follows toughness (k) and viscosity (m) dominated asymptotic behavior within 1% accuracy. For the toughness-dominated regime, the boundary is the same for both $N = 1$ and $N = 3$. The boundaries for the viscosity regime slightly differ for smaller values of leak-off and coincide for the large leak-off case. In particular, for the small leak-off case, the viscosity regime boundary for $N = 1$ shifts farther from the tip (Fig. 10a, dashed blue line). The reason is that the fracture opening for $N = 1$ is larger than the one for $N = 3$ (or very close to it) and thus the viscosity asymptote is reached farther from the tip.

As shown in Fig. 10a, the effect of bridging on the fracture opening is most noticeable in a localized area. Fig. 10b shows a close-

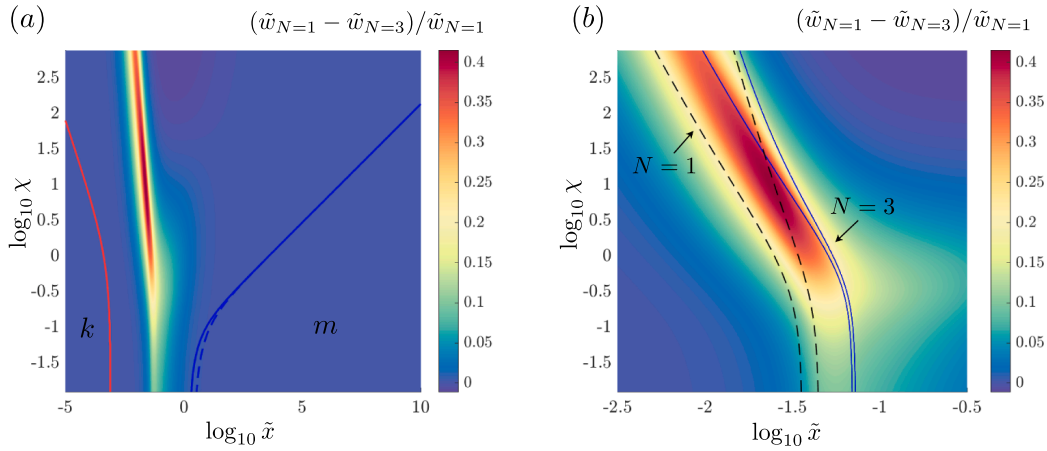


Fig. 10. The effect of bridging criterion represented by the relative difference of \tilde{w} for bridging factor $N = 1$ and $N = 3$ inside a parameter space of scaled coordinate \tilde{x} and leak-off χ (a). The larger effect appears in proximity to proppant packs shown in a zoomed plot (b) with the proppant boundaries for $N = 1$ (dashed lines) and $N = 3$ (solid lines). Toughness (k) and viscosity (m) dominated regions are outlined in (a) for $\tilde{w}_{N=1}$ (solid lines) and $\tilde{w}_{N=3}$ (dashed lines). Parameters used are the same as for Fig. 4.

up view of this area that is concentrated mostly around regions containing proppant. The dashed and solid lines in Fig. 10b correspond to proppant boundaries for $N = 1$ and $N = 3$, respectively. The left boundary for $N = 1$ (dashed line) appears closer to the tip which is consistent with the bridging criterion.

The sensitivity of the full numerical solution to bridging is illustrated in Fig. 11 for the same parameters as in Figs. 4, 10 but for the fixed value of leak-off $\chi = 10$. For smaller N , proppant is packed closer to the fracture front (Fig. 11c), which, at the constant proppant volume, causes a shift of both boundaries of packed proppant. For small N , fracture opening on the length scale of the proppant pack is larger, in consistency with Fig. 10. The pressure profile (Fig. 11d) is shifted correspondingly as well and, additionally, the pressure differs ahead of the proppant zone (closer to the tip) while right behind it the pressure is similar for both N .

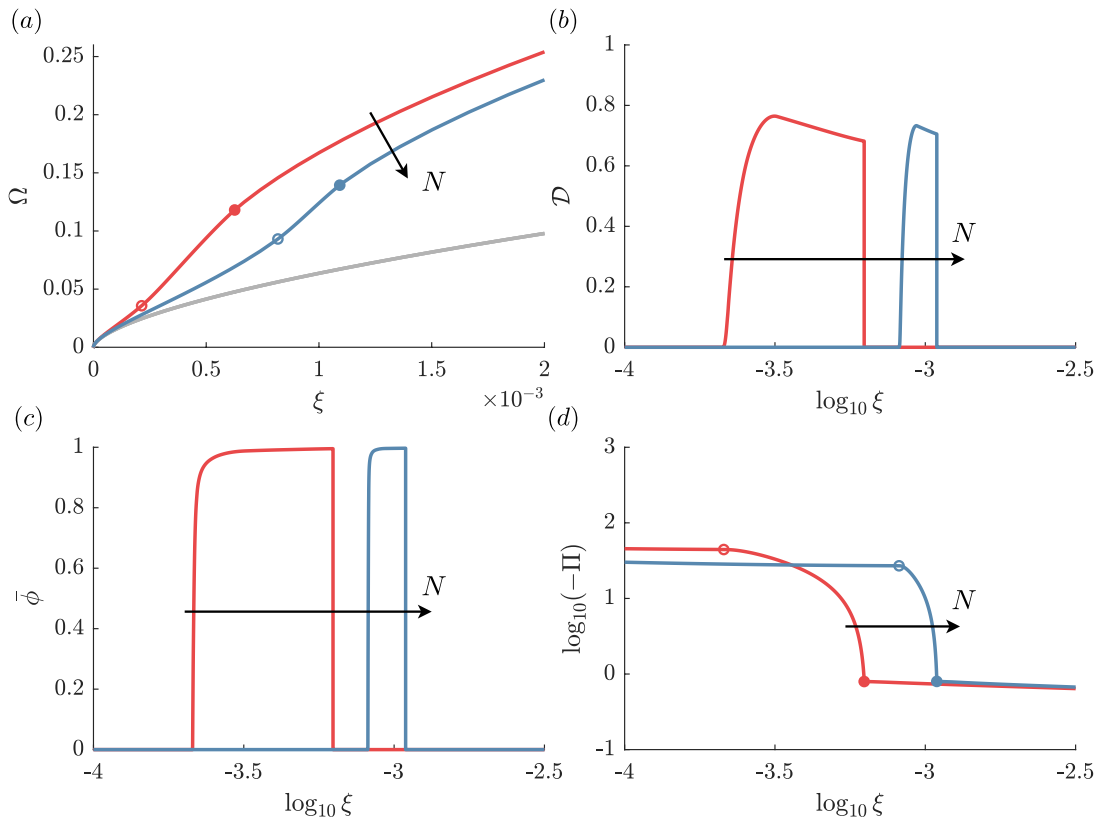


Fig. 11. Sensitivity of numerical solution to the bridging factor $N = \{1, 3\}$. Numerical solution for (a) scaled fracture opening, (b) relative effect of Darcy filtration, (c) proppant concentration, and (d) pressure. Parameters are the same as for Fig. 4 and fixed leak-off $\chi = 10$. The proppant region boundaries are indicated by circles. Gray line in (a) shows fracture opening without proppant.

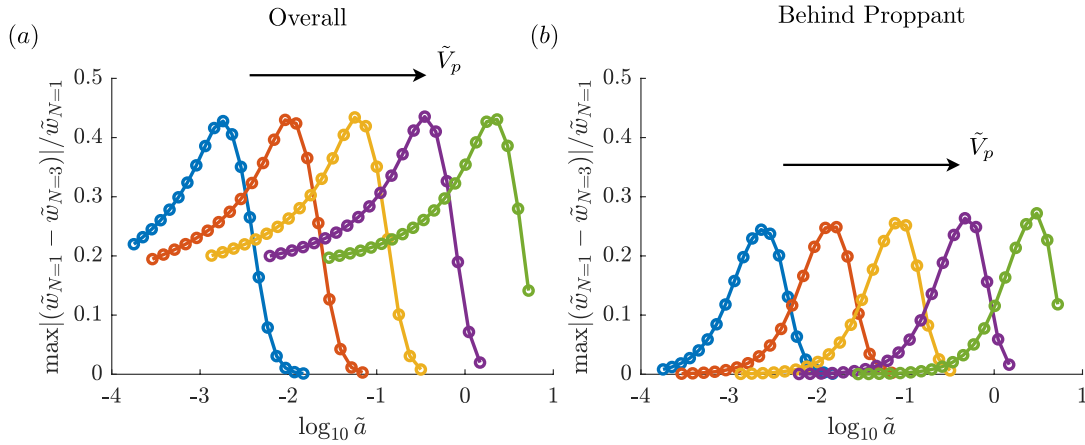


Fig. 12. Maximum relative difference between the solutions with bridging criteria at $N = \{1, 3\}$ for $D = D_m$ and large leak-off $\chi = 10^2$: (a) overall, and (b) behind the proppant pack. The results are plotted versus the dimensionless radius \tilde{a} for different volumes $\tilde{V}_p = \{10^{-8}, 10^{-6}, 10^{-4}, 10^{-2}, 1\}$.

The amplitude of the pressure jump over the proppant pack is slightly larger for small N . This makes fracture wider (Fig. 11a) bringing the maximum relative difference in the fracture opening to 41.5% overall and 21.3% for the region behind the farthest from the tip proppant pack (at $N = 3$). The filtration effect (Fig. 11b) does not change significantly with N except that its peak amplitude is a bit smaller for large N which is related to larger fracture width at which bridging occurs (Fig. 11b).

To illustrate the effect of proppant bridging for different combinations of scaled parameters \tilde{V}_p and \tilde{a} , Fig. 12a shows the relative maximum difference between solutions for different N , $\max(|\tilde{w}_{N=1} - \tilde{w}_{N=3}|)/\tilde{w}_{N=1}$. Fig. 12b shows the same quantity but focusing only on the region behind the proppant packs, $\tilde{x} > \text{maximum of } \tilde{x}_i \text{ for } N = 1 \text{ and } N = 3$. Results are computed for the large leak-off $\chi = 10^2$ and $D = D_m$.

Each plot in Fig. 12 corresponds to a particular value of the dimensionless proppant volume $\tilde{V}_p = \{10^{-8}, 10^{-6}, 10^{-4}, 10^{-2}, 1\}$. For each \tilde{V}_p , the range of \tilde{a} is determined from the diagram shown in Fig. 3 to consider physically admissible values.

Results demonstrate that the effect of the bridging factor is significant within the packed proppant zone (Fig. 12a). At the same time, behind this proppant zone the effects are reduced significantly for smaller \tilde{a} , and slightly reduced for intermediate values of \tilde{a} (Fig. 12b). The effect of bridging on the region behind the proppant zone is considered separately because a solution in this region determines the global behavior of a fracture which is of most interest for hydraulic fracturing simulations.

One interesting observation is that as \tilde{V}_p increases, the results shift mostly to the right and the shape of the curve remains almost the same. For smaller values of \tilde{a} , the effect of proppant bridging increases with \tilde{a} , then at some value it peaks, and for larger \tilde{a} it drops to zero. The latter drop to zero corresponds to the case when \tilde{a} is getting so large that the proppant pack length shrinks and the solutions for both N become equivalent to the solution without proppant. To better understand why the curves exhibit mostly shift in Fig. 12, let us first note that the relevant dimensionless parameter that quantifies the effect of proppant bridging is $(\tilde{x}_1 - \tilde{x}_0)/(\tilde{x}_0(N = 3) - \tilde{x}_0(N = 1))$, which is the scaled length of the proppant pack relative to the shift of the left boundary due to bridging criterion. Based on Eq. (34) and Eq. (37), we can provide the following estimates,

$$\tilde{x}_1 - \tilde{x}_0 \sim \frac{\tilde{V}_p}{\tilde{w}\chi^2}, \quad (\tilde{x}_0(N = 3) - \tilde{x}_0(N = 1)) \sim \frac{\tilde{a}}{\tilde{w}}. \tag{41}$$

Then we estimate these quantities at $\tilde{x} = \tilde{x}_0$, where \tilde{x}_0 is of the same order as its shift due to bridging,

$$\tilde{x}_0 \sim \frac{\tilde{a}}{\tilde{w}}. \tag{42}$$

The ratio of the quantities from Eq. (41) with using $\tilde{w} \sim x^\delta$ gives the parameter that characterizes the effect of proppant bridging,

$$\frac{\tilde{x}_1 - \tilde{x}_0}{\tilde{x}_0(N = 3) - \tilde{x}_0(N = 1)} \sim \frac{\tilde{V}_p}{\tilde{a}^r}, \quad r = \frac{3 + \delta}{1 + \delta}. \tag{43}$$

Noting from Eq. (39) that δ varies from 0 to 1/3, we have $2.5 \leq r \leq 3$, where 2.5 corresponds to using the toughness asymptote and 3 corresponds to using the viscous asymptote. Note that for the leak-off asymptote $\delta = 0.25$, and therefore, $r = 2.6$. Fig. 13 plots the same results as Fig. 12 but versus \tilde{a}^r/\tilde{V}_p at $r = 2.65$. The exponent r was obtained numerically to make the results for different scaled parameters overlap and almost collapse to a single curve. This allows to establish characteristic parameter that determines proppant bridging for the fixed leak-off. The numerically estimated exponent for the large leak-off case $r = 2.65$ is close to the theoretical value for the leak-off dominance $r = 2.6$.

To better understand the behavior corresponding to small and large effects of bridging, Fig. 14 plots the solution for scaled fracture opening \tilde{w} at $N = 1$ (black lines) and $N = 3$ (red lines) for $\tilde{V}_p = 10^{-4}$ and different values of \tilde{a} that are consistent with yellow curve in Fig. 12. Fig. 14a corresponds to the smallest considered value of \tilde{a} ($\log_{10} \tilde{a} = -2.87$) at which the effect of bridging behind the proppant pack is almost zero, i.e., solutions for $N = 1$ and $N = 3$ coincide in this region. Alternatively, Fig. 14b corresponds to the

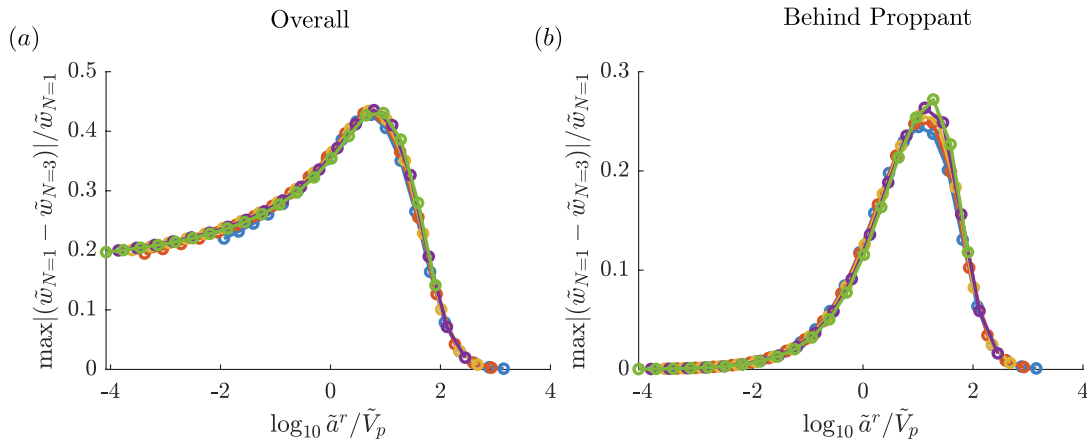


Fig. 13. Maximum relative difference between the solutions with bridging criteria at $N = \{1, 3\}$ for $D = D_m$ and large leak-off $\chi = 10^2$: (a) overall, and (b) behind the proppant pack for $\tilde{V}_p = \{10^{-8}, 10^{-6}, 10^{-4}, 10^{-2}, 1\}$ (overlapping colored lines). The results are plotted versus $\tilde{a}^r / \tilde{V}_p$ for $r = 2.65$.

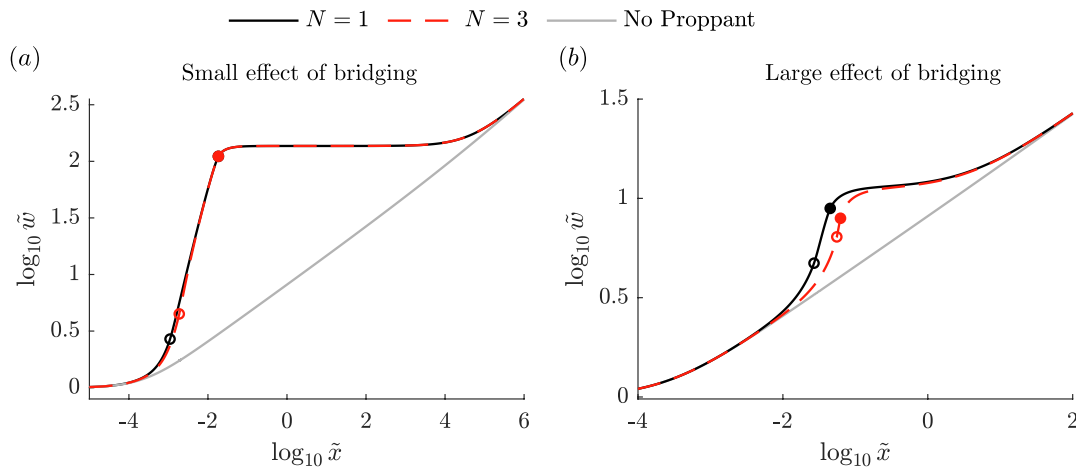


Fig. 14. The scaled fracture opening \tilde{w} versus \tilde{x} for bridging factor $N = 1$ (black line) and $N = 3$ (red line) for $\chi = 10^2$, $\tilde{V}_p = 10^{-4}$, and (a) $\log_{10} \tilde{a} = -2.87$ and (b) $\log_{10} \tilde{a} = -1.25$. These values represent the cases of (a) smaller (20% overall and 0.07% behind the proppant packs) and (b) larger (43.4% overall and 22.5% behind the proppant packs) effect of bridging factor. (For interpretation of the references to colour in this figure legend, the reader is referred to the web version of this article.)

intermediate value $\log_{10} \tilde{a} = -1.25$ at which the maximum effect of bridging is reached.

First, to explain the behavior for smaller \tilde{a} , let us recall that for smaller \tilde{a} , the proppant causes larger fracture widening as discussed in Section 6.2. In this case, a variation of the bridging factor N slightly shifts the left boundary of the proppant pack on a logarithmic scale and almost does not affect the right boundary. As a result, the bridging factor only affects the solution for \tilde{w} inside the proppant pack (20% at maximum), but it almost does not change \tilde{w} behind it (0.07% at maximum), i.e., the plateau region of \tilde{w} has the same level for both $N = 1$ and $N = 3$ (Fig. 14a). Physically, this means that if there is a large tight proppant pack, then the choice of bridging criterion does not affect the solution behind it.

With the increase of the dimensionless particle radius \tilde{a} , the pressure jump over the pack and fracture widening due to the presence of proppant decreases, therefore the overall effect of proppant is less strong. At the same time, we observe that the effect of bridging increases (Fig. 12). The solution that corresponds to the largest effect of bridging is illustrated in Fig. 14b. In this case, the maximum relative difference between \tilde{w} for $N = 1$ and $N = 3$ is 43.4% overall and 22.5% behind the proppant packs. The reason is that the effect of bridging is naturally the most relevant for determining the left boundary of the pack. In this case, the left and right boundaries are very close, and therefore the influence continues in a region behind the proppant pack as well.

To summarize, the effect of bridging is most significant when the difference between the left boundaries of the proppant pack for $N = 1$ and $N = 3$ is larger or comparable to the length of the proppant packs. This suggests that at an early time of screen-out when the proppant pack near the fracture front is relatively short, the correct choice of the bridging criterion is crucial as the solution is very sensitive to it. Later on, when the size of the proppant pack becomes larger, the effect of bridging is concentrated on the length scale of the left boundary of the proppant pack and the choice of bridging criterion does not affect the solution behind the propped region.

7. Summary

The paper presented an extensive study of the effects of proppant of varied volume and particle radius on the near-tip behavior of a hydraulic fracture. The near-tip region of the crack is modeled as a semi-infinite fracture that propagates with a constant velocity. The main conclusions are summarized as follows:

- It was determined that, when plotted on a logarithmic scale, the effects of proppant on the fracture opening appear to be localized, i.e., the solution with proppant is similar to the solution without proppant on the small length scale near the tip, and the solutions approach each other far from the proppant region. However, when plotted on a linear scale, it becomes clear that the effects of proppant will likely span along the whole crack. The primary influence of proppant is fracture widening along the region surrounding the proppant pack. Besides, the behavior away from the pack and farther from the tip is close to that corresponding to the fracture toughness dominated solution but with an effectively increased fracture toughness. Thus, a small amount of proppant near the tip results in an increase in effective fracture toughness and renders fractures shorter and wider. Further away from the tip, the behavior transitions to leak-off and/or viscosity dominated solutions depending on the problem parameters. Additionally, the proppant introduces a noticeable jump of the fluid pressure through the proppant pack.
- Larger proppant volumes and smaller particle sizes, as expected, cause a more significant pressure jump and fracture widening. Smaller particles decrease the permeability of the proppant pack, which in turn increases the effect. In addition, smaller particles shift the location of the proppant closer to the fracture tip due to bridging. The extent of these effects is quantified.
- The transition between the Poiseuille flow of slurry at low proppant concentration and Darcy filtration of clear fluid through the pack at high proppant concentration is based on the proppant transport model derived earlier based on the experimental observations. The relative effect of Darcy filtration is found to be the most sensitive to fluid leak-off, with larger leak-off values leading to a more significant contribution of filtration. Additionally, the influence of filtration reaches its peak at the onset of the proppant pack and then decreases with distance from the tip as fracture width increases.
- The sensitivity of the solution to the choice of a bridging criterion is investigated by varying the bridging factor – a ratio of fracture opening to proppant size at which bridging occurs. For smaller factors, bridging occurs closer to the tip and is associated with larger pressure jump over the pack and larger fracture widening. The effect of bridging criterion on the fracture behavior behind the proppant zone is significant when the length of the proppant pack is less or comparable to the shift of the left boundary of the pack due to change of the bridging criterion. Otherwise, the bridging criterion does not noticeably affect the solution behind the proppant.

Declaration of Competing Interest

The authors declare that they have no known competing financial interests or personal relationships that could have appeared to influence the work reported in this paper.

Acknowledgements

The support of the University of Houston in the form of a research assistantship to A.B. is acknowledged.

References

- [1] Adachi J, Siebrits E, Peirce A, Desroches J. Computer simulation of hydraulic fractures. *Int J Rock Mech Min Sci* 2007;44:739–57.
- [2] Barbati AC, Desroches J, Robisson A, McKinley GH. Complex fluids and hydraulic fracturing. *Annu Rev Chem Biomol Eng* 2016;7:415–53.
- [3] Belyadi H, Fathi E, Belyadi F. Hydraulic fracturing in unconventional reservoirs: theories, operations, and economic analysis. Elsevier Science & Technology; 2016.
- [4] Berg RR. Method for determining permeability from reservoir rock properties. *Trans Gulf Coast Assoc Geol Soc* 1970;20:303–17.
- [5] Bessmertnykh AO, Dontsov EV. Analysis of a hydraulic fracture's tip region with proppant plug. 51st US Rock Mechanics/Geomechanics Symposium. American Rock Mechanics Association; 2017.
- [6] Bessmertnykh AO, Dontsov EV. A semi-infinite hydraulic fracture driven by a Herschel-Bulkley fluid. *J Appl Mech* 2019;1–16.
- [7] Boronin SA, Osipov AA. Two-continua model of suspension flow in a hydraulic fracture. *Doklady physics*. 55. Springer; 2010. p. 199–202.
- [8] Boyer F, Guazzelli E, Pouliquen O. Unifying suspension and granular rheology. *Phys Rev Lett* 2011;107(18):188301.
- [9] Carman PC. Fluid flow through granular beds. *Trans Inst Chem Eng* 1937;15(150–166).
- [10] Carter ED. Optimum fluid characteristics for fracture extension. In: Howard GC, Fast CR, editors. *Drilling and production practices*. 1957. p. 261–70.
- [11] Chekhonin E, Levonyan K. Hydraulic fracture propagation in highly permeable formations, with applications to tip screenout. *Int J Rock Mech Min Sci* 2012;50:19–28.
- [12] Denn MM, Morris JF. Rheology of non-Brownian suspensions. *Annu Rev Chem Biomol Eng* 2014;5:203–28.
- [13] Desroches J, Detournay E, Lenoach B, Papanastasiou P, Pearson J, Thiercelin M, Cheng A-D. The crack tip region in hydraulic fracturing. *Proc R Soc Lond A* 1994;447:39–48.
- [14] Detournay E. Mechanics of hydraulic fractures. *Annu Rev Fluid Mech*; 2016.
- [15] Dontsov E, Peirce A. A new technique for proppant schedule design. *Hydraulic Fract J* 2014;1(3):8–15.
- [16] Dontsov E, Peirce A. A non-singular integral equation formulation to analyze multiscale behaviour in semi-infinite hydraulic fractures. *J Fluid Mech* 2015;781:R1.
- [17] Dontsov EV, Boronin SA, Osipov AA, Derbyshev DY. Lubrication model of suspension flow in a hydraulic fracture with frictional rheology for shear-induced migration and jamming. *Proc Royal Soc A* 2019;475(2226):20190039.
- [18] Dontsov EV, Kresse O. A semi-infinite hydraulic fracture with leak-off driven by a power-law fluid. *J Fluid Mech* 2018;837:210–29.
- [19] Dontsov EV, Peirce AP. Slurry flow, gravitational settling, and a proppant transport model for hydraulic fractures. *J Fluid Mech* 2014;760:567–90.

- [20] Dontsov EV, Peirce AP. Proppant transport in hydraulic fracturing: crack tip screen-out in KGD and P3D models. *Int J Solids Struct* 2015;63:206–18.
- [21] Economides MJ, Nolte KG, editors. *Reservoir Stimulation*. 3rd Edition Chichester, UK: John Wiley & Sons; 2000.
- [22] Eskin D, Miller MJ. A model of non-newtonian slurry flow in a fracture. *Powder Technol* 2008;182(2):313–22.
- [23] Garagash DI, Detournay E, Adachi JI. Multiscale tip asymptotics in hydraulic fracture with leak-off. *J Fluid Mech* 2011;669:260–97.
- [24] Garagash IA, Osipov AA, Boronin SA. Dynamic bridging of proppant particles in a hydraulic fracture. *Int J Eng* 2019;135:86–101.
- [25] Gidaspow D. *Multiphase flow and fluidization: continuum and kinetic theory descriptions*. Academic Press; 1994.
- [26] Guazzelli E, Morris JF. *A physical introduction to suspension dynamics* vol. 45. Cambridge University Press; 2011.
- [27] Irwin G. Analysis of stresses and strains near the end of a crack traversing a plate. *J Appl Mech* 1957;24:361–4.
- [28] Kozeny J. Ueber kapillare leitung des wassers im boden. *Sitzungsber Akad. Wiss., Wien* 1927;136(2a):271–306.
- [29] Krumbein W, Monk G. Permeability as a function of size parameters of unconsolidated sand. *AIME* 1943;151(1):153.
- [30] Lecampion B, Garagash DI. Confined flow of suspensions modelled by a frictional rheology. *J Fluid Mech* 2014;759:197–235.
- [31] Leighton D, Acrivos A. The shear-induced migration of particles in concentrated suspensions. *J Fluid Mech* 1987;181:415–39.
- [32] Lenoach B. The crack tip solution for hydraulic fracturing in a permeable solid. *J Mech Phys Solids* 1995;43:1025–43.
- [33] Lutynski M, Janus D, Zimny M. Comparison of selected properties of natural and ceramic proppants used in hydraulic fracturing technologies. *J Polish Mineral Eng Soc* 2015;2:299–303.
- [34] Morris JF, Boulay F. Curvilinear flows of noncolloidal suspensions: the role of normal stresses. *J Rheol* 1999;43(5):1213–37.
- [35] Nott PR, Brady JF. Pressure-driven flow of suspensions: simulation and theory. *J Fluid Mech* 1994;275:157–99.
- [36] Osipov AA. Fluid mechanics of hydraulic fracturing: a review. *J Petrol Sci Eng* 2017;156:513–35.
- [37] Osipov AA. Hydraulic fracture conductivity: effects of rod-shaped proppant from lattice-Boltzmann simulations and lab tests. *Adv Water Resources* 2017;104:293–303.
- [38] Ovarlez G, Bertrand F, Rodts S. Local determination of the constitutive law of a dense suspension of non-colloidal particles through magnetic resonance imaging. *J Rheol* 2006;50(3):259–92.
- [39] Pearson JRA. On suspension transport in a fracture: framework for a global model. *J Non-Newton Fluid* 1994;54:503–13.
- [40] Peirce A, Detournay E. An implicit level set method for modeling hydraulically driven fractures. *Comput Meth Appl Mech Eng* 2008;197:2858–85.
- [41] Rice JR. A path independent integral and the approximate analysis of strain concentration by notches and cracks. *J Appl Mech* 1968;35:379–86.
- [42] Richardson JF, Zaki WN. Sedimentation and fluidization: part I. *Trans Inst Chem Eng* 1954;32:35–47.
- [43] Roper SM, Lister JR. Buoyancy-driven crack propagation: the limit of large fracture toughness. *J Fluid Mech* 2007;580:359–80.
- [44] Spence DA, Sharp PW, Turcotte DL. Buoyancy-driven crack propagation: a mechanism for magma migration. *J Fluid Mech* 1987;174:135–53.
- [45] Stickel JJ, Powell RL. Fluid mechanics and rheology of dense suspensions. *Annu Rev Fluid Mech* 2005;37:129–49.